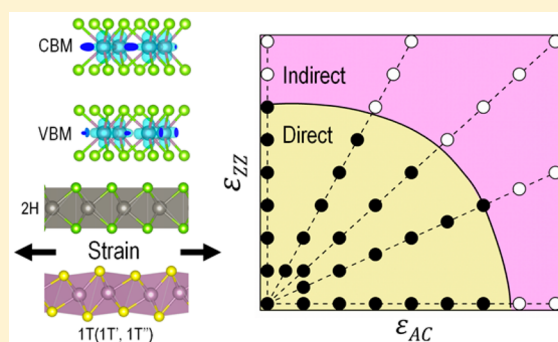# Bandgap Transition of 2H Transition Metal Dichalcogenides: Predictive Tuning via Inherent Interface Coupling and Strain

Bin Ouyang,[†] Zetian Mi,[‡] and Jun Song[*],[†]

[†]Department of Mining and Materials Engineering and [‡]Department of Electrical and Computer Engineering, McGill University, Montreal, QC H3A 0G4, Canada

S *Supporting Information*

ABSTRACT: Phase transitions within two-dimensional transition metal dichalcogenides (TMD) promise new possibilities for engineering their properties. Using first-principles density functional theory (DFT) calculations, we systematically examined the interfacial electronic coupling between the 2H phase monolayer with its polymorphic phases in several group IV TMD, i.e., MoS_2 ($MoSe_2$) and WS_2 (WSe_2), inherent bilayer heterostructures. It is found that the interface coupling, augmented by in-plane strain, can greatly modify the band structure of the 2H phase to induce bandgap transition (either indirect-to-direct or direct-to-indirect). Moreover, the effects of strain on the band structure can be well understood and predicted within the framework of deformation potential theory. The present study provides important insights toward engineering optoelectronic properties of TMD-based devices.

1. INTRODUCTION

Monolayer and few-layer transition metal dichalcogenides (TMDs) have emerged as an important group of two-dimensional (2D) materials because of their particular potential in applications such as optoelectronic devices,[1−6] valleytronics,[7−9] field effect transistors,[10−14] piezoelectric devices,[15−18] and thermoelectric devices.[19−23] Typical representatives of the TMD family include the group VI dichalcogenides, MX_2 (M = Mo or W and X = S or Se). A MX_2 nanosheet consists of X−M−X triple atomic planes, bonded together by van der Waals forces. As its thickness varies, a group IV TMD nanosheet can exhibit either an indirect (e.g., multilayer MoS_2) or direct bandgap (e.g., monolayer MoS_2),[24] indicating the importance of interlayer coupling in affecting the band structure. This suggests the important role of interlayer coupling in modifying the band structures of TMDs, and stimulates numerous studies to investigate stacked TMD heterostructures.[6,19,25−28] The heterostructure can be constructed by layers of different TMD materials that are of the same lattice structure (e.g., MoS_2/WS_2, $MoSe_2/WSe_2$)[25,27,29] or be a combination of a TMD material with other 2D material(s) of distinct lattice structures (e.g., MoS_2/graphene, MoS_2/h-BN).[30−32] For the first category, the electronic states of different materials within the heterostructure are fully mixed[2,11,39,40,64] due to structural coherence across the interface, while for the second category the electronic states of different materials are largely decoupled[30−32] because of the structural heterogeneity across the interface. Those TMD heterostructures enable flexible engineering of electronic and

phonon properties to promise a wide range of applications.[25,27,29−32]

Recently, the probing of multiple phases in 2D TMD systems provides some new aspects. It has been shown that intercalation,[33−37] doping,[38−42] or deformation[29,40,43] can controllably induce phase transitions in group IV TMDs between trigonal prismatic (2H phase) and its allotropes (1T, 1T′, and 1T″ phases). Those allotropic phases are compositionally the same as the 2H phase but of different lattice structures. In particular, 1T has a octahedral structure while 1T′ and 1T″ assume distorted octahedral structures with zigzag chain and tetragonal superlattice of Mo atoms, respectively.[40] The distinction in the lattice structure leads to different properties[33,34,44−47] for those phases. This brings the possibility of inherent TMD heterostructures. Different from those conventional heterostructures that consist of two or more materials types, the inherent heterostructures are on one hand structurally dissimilar across the interface while on the other compositionally the same. Moreover, recent advances in the synthesis of TMD make it possible to selectively induce phase transformation on specific monolayer(s) within TMD.[34,37,40,48−50] This makes it possible to fabricate inherent TMD heterostructures without the complexity of manipulating/stabilizing individual monolayer TMD sheets, thus promising great advantages than those noninherent TMD heterostructures that are challenging in fabrication. Meanwhile

those heterostructures have been shown to be stable under ambient conditions and thus can be readily used in devices.[34,36,40] Therefore, inherent TMD heterostructures provide appealing new additions to the 2D TMD family.

In the present study, we employ first-principles density functional theory (DFT) calculations to study the bilayer MX_2 (M = Mo or W and X = S or Se) inherent heterostructures. The effects of interface coupling together with the in-plane strain on the electronic properties of the $2H\text{-}MX_2$ have been systematically examined. The strain was found to induce band shifting and bending and influence the competition between K−K and Γ−K energy gaps of the interface-influenced $2H\text{-}MX_2$, resulting in bandgap transition from direct gap to indirect gap, or vice versa. Based on the deformation potential theory, an analytic model was then formulated and parametrized to predictively map the strain domains that correspond to direct and indirect bandgaps. Our results provide new insights toward predictive engineering and design of TMD-based nanophotonic devices.

2. COMPUTATIONAL METHODOLOGY

First-principles DFT calculations employing the Perdew−Burke−Ernzerhof (PBE) functional[51] and projector augmented-wave (PAW)[52] method were performed using the Vienna *ab initio* simulation package (VASP).[24] For each calculation, a supercell enclosing an inherent bilayer MX_2 heterostructure was constructed. The heterostructure consists of one 2H phase MX_2 (i.e., noted as $2H\text{-}MX_2$ below) monolayer of 2 × 2 supercell sitting on top of its octahedral allotrope, denoted as $1T^\psi$, of the same dimension, with $1T^\psi$ being 1T, 1T′, or 1T″,[53] as illustrated in Figure 1. Benchmark
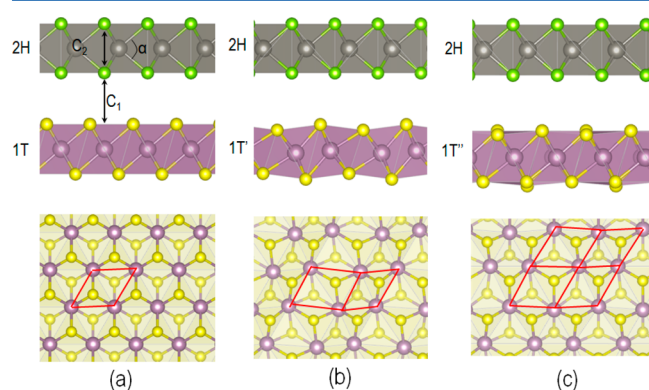

Figure 1. Ground-state configurations of bilayer MX_2: (a) 2H/1T, (b) 2H/1T′, and (c) 2H/1T″ heterostructures. The M (metal) and X (chalcogen) atoms are represented by large gray/purple and blue/yellow spheres, respectively. The parameters C_1, C_2, and α denote the separation between the 2H phase and its octahedral allotrope, the vertical separation between X atoms within the 2H phase, and the angle between two adjacent M−X bonds. The red grid lattice indicates the unit cell of 1T, 1T′, and 1T″ phase, respectively.

calculations have been performed using larger supercells to ensure no size dependence of our results. For each $2H/1T^\psi$ combination, four different stacking sequences exist, and the one of the lowest energy was studied. Furthermore, in this study we only consider those $2H/1T^\psi$ heterostructures that derive from a 2H bilayer (through, e.g., phase transformation in one monolayer), and thus there is no relative rotation between adjacent monolayers.

From Figure 1, we see that the 1T phase can be regarded as a structural transition of 2H phase where the X atoms on one

side of the M atoms are shifted to coincide (in the projection view) with the centers of the hexagons formed by M atoms and other X atoms (cf. Figure 1a). This transition results in a change of the symmetry from $P6_3/mmc$ to $P3$. The 1T′ and 1T″ phases, on the other hand, are induced by further distortions of the M chain,[40,54] which has been proved to be more stable in experimental observations.[53,55] (cf. Figure 1b,c).

The dispersive van der Waals interactions between the two monolayers were included using the DFT-D2 method of Grimme.[56−58] The vertical spacing between the bilayer and its adjacent image was set to be larger than 1.8 nm to eliminate periodic image interactions. A 7 × 7 × 1 k-point grid and cutoff energy of 400 eV were used. Noncollinear magnetic calculations were performed to capture spin−orbital coupling (SOC) induced splitting.[7,24,59−61] The properties and responses of those $2H/1T^\psi$ heterostructures, when subjected to in-plane strain, are investigated. The strain is applied to both layers; i.e., the $2H/1T^\psi$ heterostructure deforms as a whole.

3. RESULTS AND DISCUSSION

3.1. Atomic Configurations of $2H/1T^\psi$ Heterostructures.
The ground states of inherent $2H/1T^\psi$ heterostructures for different TMDs were obtained, with the corresponding lattice parameters listed in Table 1, where a_0 is the equilibrium

Table 1. Lattice Parameters (i.e., a_0, C_1, C_2, and α) of Inherent $2H/1T^\psi$ Heterostructures for Different MX_2 (M = Mo or W and X = S or Se) Systems[a]

system	heterostructure	a_0 (Å)	C_1 (Å)	C_2 (Å)	α (deg)
MoS$_2$	2H/1T	3.18	3.26	3.13	80.82
	2H/1T′		3.28		
	2T/1T″		3.44		
	2H/2H		3.68		
MoSe$_2$	2H/1T	3.33	3.35	3.33	81.61
	2H/1T′		3.20		
	2T/1T″		3.23		
	2H/2H		3.45		
WS$_2$	2H/1T	3.18	3.17	3.13	80.91
	2H/1T′		3.09		
	2T/1T″		2.77		
	2H/2H		2.99		
WSe$_2$	2H/1T	3.33	3.10	3.33	81.56
	2H/1T′		2.96		
	2T/1T″		2.93		
	2H/2H		3.10		

[a]The relative parameters of corresponding 2H bilayers are also listed as references.

lattice constant of the 2H phase, C_1 denotes the separation between the 2H phase and its octahedral allotrope, C_2 denotes the vertical separation between X atoms within the 2H phase, and α is the angle between two adjacent M−X bonds (cf. Figure 1a). From Table 1, we note that for the same TMD the values of C_2 and α remain invariant for $2H/1T^\psi$ heterostructures, consistent with previous studies.[24,62] It can also be seen that MoS$_2$ and WS$_2$, and MoSe$_2$ and WSe$_2$, respectively, have almost exactly the same monolayer lattice parameters, i.e., a_0, C_2, and α, again in agreement with previous studies.[26,27,54,55] However, different heterostructures show noticeably different values of the interlayer separation C_1 (even among the ones of the same TMD). This suggests that these structures exhibit

distinct long-range dispersive interactions and possibly different interface coupling between 2H and $1T^{\psi}$ phases.

3.2. Interface-Influenced Electronic Properties of 2H Phases.
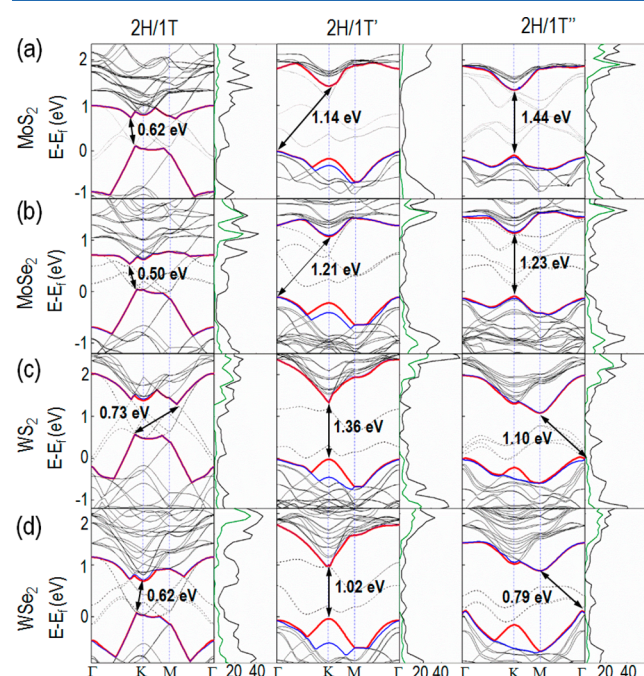
Figure 2 shows the band structures and corresponding

Figure 2. Band structure and corresponding PDOS plots for bilayer (a) MoS$_2$, (b) MoSe$_2$, (c) WS$_2$, and (d) WSe$_2$ inherent heterostructures with corresponding PDOS. All the energy levels are with reference to the Fermi energy. The CBM and VBM bands corresponding to the 2H phase are colored red, while the blue curves indicate the corresponding splitting bands of CBM/VBM. Other bands with 2H states are indicated by solid black lines while the rest are indicated by dotted black lines. The 2H bandgap in each case is indicated by the brown arrow and text. In the PDOS plot, the black line represents the total DOS while the green line represents DOS coming from the 2H phase.

projected density of states (PDOS) of inherent $2H/1T^{\psi}$ heterostructures for different TMDs. It is apparent from the density of states (DOS) contributed by the 2H phase (colored green in Figure 2) reveal a much larger gap than the overall bandgap. The effective conduction band minimum (CBM) and valence band maximum (VBM) corresponding to the 2H phase are identified, indicated by red curves in Figure 2. Thereby the effective bandgap of the 2H phase, modified by the interface coupling between 2H and $1T^{\psi}$ phases, can be obtained, shown in Table 2. We can note from Table 2 that there is a significant dependence of the effective bandgap on the $2H/1T^{\psi}$ interface type. Particularly the effective bandgap exhibits the lowest value in the heterostructure with the 2H/1T interface. This interface

dependence can be understood by examining the highest occupied molecular orbital (HOMO) for the 2H phase. In the 2H/1T heterostructure, the HOMO for the 2H phase is constituted by bands with hybridized 2H and 1T states. These bands are significantly elevated comparing to the one in free-standing 2H TMD monolayer,[25,63] thus leading to a large reduction in the bandgap. The hybridization of 2H and 1T′ (or 1T″) states also exist in the 2H/1T′ (or 2H/1T″) heterostructures, although the HOMO remains to be the same orbital as the one in the free-standing 2H-MX$_2$ monolayer.[25,63] Nonetheless, certain reduction in the bandgap (with reference to the free-standing 2H phase) still occurs because of sizable band bending. Besides altering the effective bandgap, the band bending also induces bandgap transitions between direct gap and indirect gap, or vice versa (cf. Figure 2 and Table 2). Specifically, we note that for MoS$_2$ and MoSe$_2$ the 2H/1T and 2H/1T′ interface couplings induce direct to indirect transitions while the 2H phase stacked on 1T″ maintains a direct bandgap, yet for WS$_2$ and WSe$_2$, the 2H/1T and 2H/1T″ interface couplings induce direct to indirect transitions while the 2H phase stacked on 1T′ maintains a direct bandgap. Meanwhile, spin−orbital splitting of CBM and VBM was observed (see Figure 2, where the splitting bands indicated by thin blue lines), and the corresponding magnitude of energy splitting at the K point is listed in Table 2. It is apparent from the data in Table 2 that the spin−orbital splitting is also greatly influenced by the $2H/1T^{\psi}$ interface coupling.

To further understand the role of interface coupling, the partial charge distributions at CBM and VBM were calculated for different systems, shown in Figure 3 with MoS$_2$ and WS$_2$ selected as the representatives. MoS$_2$ and MoSe$_2$, and WS$_2$ and WSe$_2$, respectively were found to exhibit similar partial charge distributions, which is well expected given their close structural and chemical resemblance (see Supporting Information for details). Thus, in our discussion below they are grouped as MoS$_2$ (MoSe$_2$) and WS$_2$ (WSe$_2$). As illustrated in Figure 3 (and Figure S1 in Supporting Information), MoS$_2$ (MoSe$_2$) and WS$_2$ (WSe$_2$) exhibit similar partial charge distributions at VBM and CBM in the case of 2H/1T since the CBMs occupied mainly by 3d orbitals of M (M = Mo or W) while VBMs occupied by both 3p orbitals of X (X = S or Se) and 3d orbitals of M atoms. This is consistent with the similar band shifting and energy dispersion behaviors at HOMO and LUMO corresponding to 2H phases in 2H/1T heterostructures observed in Figure 2. On the other hand, the partial charge distributions are vastly different for MoS$_2$ (MoSe$_2$) and WS$_2$ (WSe$_2$) in the cases of 2H/1T′ and 2H/1T″. This difference echoes with the distinct band shifting behaviors for MoS$_2$ (MoSe$_2$) and WS$_2$ (WSe$_2$) observed in Figure 2, where we note the VBM is located at Γ (2H/1T′) and K (2H/1T″) for MoS$_2$ (MoSe$_2$), but at K (2H/1T′) and Γ (2H/1T″) for WS$_2$ (WSe$_2$).

Table 2. Effective Bandgap of 2H-MX$_2$ (M = Mo or W and X = S or Se), Modified by the $2H/1T^{\psi}$ Interface Coupling[a]

system	2H (ML)	2H (BL)	2H (1T)	2H (1T′)	2H (1T″)
MoS$_2$	1.60[DB] (0.15)	1.47[IB] (0.15)	0.62[IB] (0)	1.14[IB] (0.15)	1.44[DB] (0.04)
MoSe$_2$	1.30[DB] (0.19)	1.23[IB] (0.17)	0.50[IB] (0)	1.21[IB] (0.19)	1.23[DB] (0.04)
WS$_2$	1.55[DB] (0.43)	1.29[IB] (0.44)	0.73[IB] (0)	1.36[DB] (0.45)	1.10[IB] (0.26)
WSe$_2$	1.19[DB] (0.47)	1.16[IB] (0.48)	0.62[IB] (0)	1.02[DB] (0.47)	0.79[IB] (0.46)

[a]2H (ML) and 2H (BL) denote the cases of 2H monolayer and bilayer, respectively. The superscripts DB and IB indicate the bandgap being direct and indirect, respectively. The values in the parentheses correspond to the spin−orbital interaction induced splitting.
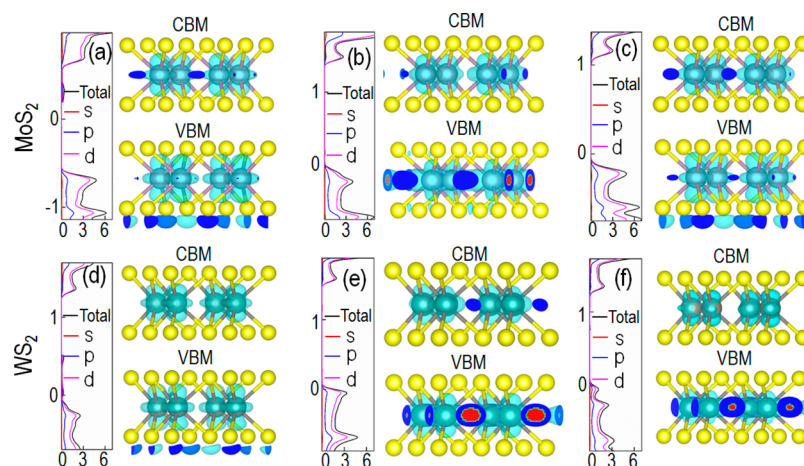
Figure 3. Conduction and covalent band edge calculations for 2H-MoS$_2$ in (a) 2H/1T, (b) 2H/1T′, and (c) 2H/1T″ bilayer heterostructures and for 2H-WS$_2$ in (d) 2H/1T, (e) 2H/1T′, and (f) 2H/1T″ bilayer heterostructures. In each subfigure, the orbital projected DOS plot (left) and orbital charge contribution of VBM and CBM (right) are shown.

The above phenomenon obtained clearly indicate that the band structure and absorption properties of 2H-MX$_2$ will be greatly altered with the influence of the octahedral phases (1T, 1T′, and 1T″), which are different from either homogeneous or heterogeneous heterostructures described above. More specifically, for both 2H-MoS2 and 2H-MoSe2 monolayer, the band gap will remain direct with the interface of 2H/1T′ existing, and at the same time gap energy will be largely altered according previous analysis of electronic structure. In the cases of 2H-WS$_2$ and 2H-WSe$_2$, the 2H monolayer will maintain a direct bandgap but with modified gap energy in the presence of the 2H/1T″ interface. The results shown in Figures 2 and 3 evidence profound effects of inherent phase interfaces on band structures of 2H-MX$_2$, promising interesting opportunities in tuning the absorption properties.

3.3. Strain Engineering of Inherent 2H/1T$^\psi$ Heterostructures. Elastic strain distorts the TMD lattice and modifies sublattice symmetry, therefore necessarily influencing the interface coupling within the 2H/1T$^\psi$ heterostructure. This coupling may further extend the tunable space for band structures of 2H/1T$^\psi$ heterostructures. In particular, the effects of biaxial strain and uniaxial strain along the AC direction and uniaxial strain along the ZZ direction are examined. Below these strains are denoted as ε_B, ε_{AC}, and ε_{ZZ}, respectively, for simple notation. Figures 4–6 show the energy gaps of interface modified 2H-MX$_2$ upon the application of ε_B, ε_{AC}, and ε_{ZZ}, respectively. To avoid the complexity of mechanical instability, only tensile strains are considered in our study. We can note that overall the energy gap decreases as strain increases [except for the case of 2H-MoSe$_2$ with 2H/1T′ interface coupling where a slight increase in the bandgap is observed (under uniaxial strain <0.005)]. Also, nonlinear dependence of the bandgap on the strain is observed at large strains. In section 3.4 we will show that the nonlinearity comes from the high-order terms in the strain-induced perturbation of Hamiltonian.

Meanwhile, crossovers between the evolutions of the energy gap for different optical energy transitions are observed. The crossover effectively results in an important phenomenon, i.e., the bandgap transition, either indirect-to-direct or direct-to-indirect, which is further elucidated in Figure 7 where the ranges of strains that correspond to direct and indirect bandgaps for different 2H-MX$_2$ are indicated. From Figure 7 we can see that there exist multiple strain regimes where the
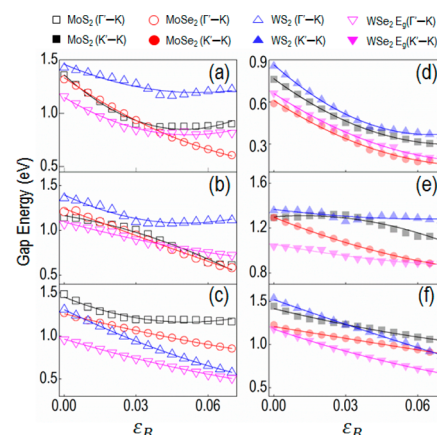

Figure 4. In-plane biaxial strain (ε_B) induced evolution of the Γ′−K gap of 2H-MX$_2$ on top of the (a) 1T, (b) 1T′, and (c) 1T″ phases and the K′−K gap of 2H-MX$_2$ on top of the (d) 1T, (e) 1T′, and (f) 1T″ phases, in MoS$_2$, MoSe$_2$, WS$_2$, and WSe$_2$ 2H/1T$^\psi$ heterostructures. The solid lines demonstrate the fitting curve from deformation potential theory.

interface modified 2H-MX$_2$ exhibits a direct bandgap. Additionally we found that the achievable range of direct bandgap is expanded in comparison to the one of monolayer 2H-MX$_2$ (details in Supporting Information). The above findings indicate that the inherent 2H/1T$^\psi$ heterostructure, together with strain engineering, provides a good viable means to realize direct bandgap beyond the TMD monolayer.

3.4. Predictive Deformation Potential Theory. On the basis of the band gap calculations, it is found that the optical energy gap transitions shown in Figure 7 mainly originate from the strain-induced band bending that leads to relocation of VBM and/or CBM among different reciprocal sites. Hence, to elucidate these transitions, we examine the effects of strain at selected high-symmetry points in the Brillouin zone. In particular, we focus on Γ′ and K′ point of the valence band edge and K point of the conduction band edge because the Γ′−K gap and K′−K gap correspond to the multilayer and monolayer behaviors respectively for 2H-MX$_2$.

The variation of Γ′−K and K′−K gaps versus strain can be analyzed within the framework of deformation potential theory.[61,64−67] Under the influence of external strain, the
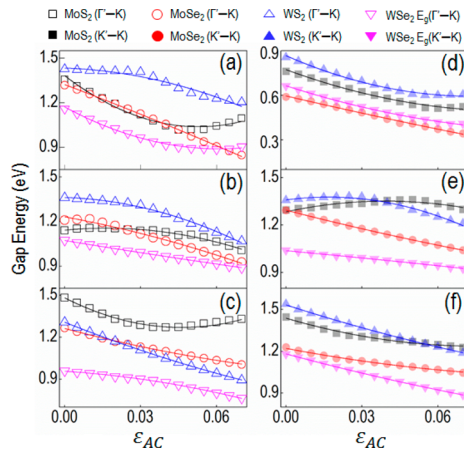
Figure 5. Evolution, induced by the in-plane uniaxial strain along the armchair direction (i.e., ε_{AC}), of the Γ'−K gap of 2H-MX$_2$ on top of the (a) 1T, (b) 1T′, and (c) 1T″ phases and the K′−K gap of 2H-MX$_2$ on top of the (d) 1T, (e) 1T′, and (f) 1T″ phases, in MoS$_2$, MoSe$_2$, WS$_2$, and WSe$_2$ 2H/1T$^\psi$ heterostructures. The solid lines demonstrate the fitting curve from deformation potential theory.
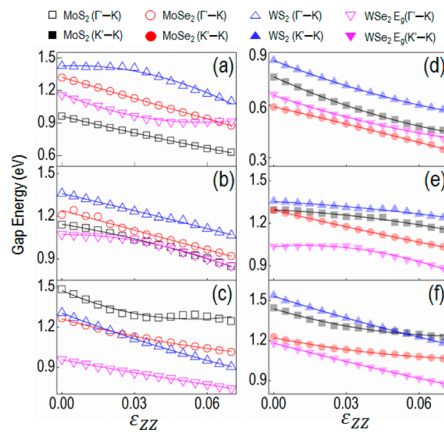
Figure 6. Evolution, induced by the in-plane uniaxial strain along the zigzag direction (i.e., ε_{ZZ}) of the Γ'−K gap of 2H-MX$_2$ on top of the (a) 1T, (b) 1T′, and (c) 1T″ phases and the K′−K gap of 2H-MX$_2$ on top of the (d) 1T, (e) 1T′, and 1T″ phases, in MoS$_2$, MoSe$_2$, WS$_2$, and WSe$_2$ 2H/1T$^\psi$ heterostructures. The solid lines demonstrate the fitting curve from deformation potential theory.

Hamiltonian of electrons in MoS$_2$ inherent heterostructures can be expressed as

$$H = H_0 + H_{SO} + H_\varepsilon \qquad (1)$$

where H_0, H_{SO}, and H_ε denote the Hamiltonian of ground state, spin−orbital interaction variation, and strain-induced perturbation of Hamiltonian, respectively. As reported in previous studies[57,61,67,68] for TMD systems (and other semiconductor systems), the H_{SO} term is ignorable compared to H_ε. Thus, we have

$$H \approx H_0 + H_\varepsilon \qquad (2)$$

The term H_ε can be expressed as

$$H_z = -\frac{\hbar^2}{2m}(\tilde{\nabla}^2 - \nabla^2) + [V(\tilde{\mathbf{r}}) - V(\mathbf{r})] \qquad (3)$$

where $\mathbf{r} = (r_1, r_2, r_3)$ and $\tilde{\mathbf{r}} = (\tilde{r}_1, \tilde{r}_2, \tilde{r}_3)$ are position vectors prior to and post deformation, V denotes the potential energy, and

$$\tilde{\nabla} = \left(\frac{\partial}{\partial \tilde{r}_1}, \frac{\partial}{\partial \tilde{r}_2}, \frac{\partial}{\partial \tilde{r}_3}\right) \quad \text{and} \quad \nabla = \left(\frac{\partial}{\partial r_1}, \frac{\partial}{\partial r_2}, \frac{\partial}{\partial r_3}\right) \qquad (4)$$

The first and second terms in eq 3 represent the strain-induced perturbations in kinetic energy and potential energy, respectively, and are thereafter denoted as H_ε^K and H_ε^P for simplicity. Considering a TMD system subjected to two normal engineering strains, ε_{AC} and ε_{ZZ}, along AC and ZZ directions, respectively, we can obtain omitting high-order (i.e., third-order or above) terms (see Supporting Information for details)

$$H_\varepsilon^K \approx -\frac{\hbar^2}{2m}\left[(-2\varepsilon_{AC} + 3\varepsilon_{AC}^2)\frac{\partial^2}{\partial r_1^2} + (-2\varepsilon_{ZZ} + 3\varepsilon_{ZZ}^2)\frac{\partial^2}{\partial r_2^2}\right] \qquad (5)$$

and

$$H_\varepsilon^P \approx \left(\frac{\partial V}{\partial r_1}r_1\right)\varepsilon_{AC} + \left(\frac{\partial V}{\partial r_2}r_2\right)\varepsilon_{ZZ} + \left(\frac{\partial V}{\partial r_1}r_1^2\right)\varepsilon_{AC}^2$$
$$+ \left(\frac{\partial V}{\partial r_2}r_2^2\right)\varepsilon_{ZZ}^2 + 2\left(\frac{\partial V}{\partial r_1 \partial r_2}r_1 r_2\right)\varepsilon_{AC}\varepsilon_{ZZ} \qquad (6)$$

Therefore, we have

$$H_\varepsilon = \left(\frac{\hbar^2}{m}\frac{\partial^2}{\partial r_1^2} + \frac{\partial V}{\partial r_1}r_1\right)\varepsilon_{AC} + \left(\frac{\hbar^2}{m}\frac{\partial^2}{\partial r_2^2} + \frac{\partial V}{\partial r_2}r_2\right)\varepsilon_{ZZ}$$
$$+ \left(-\frac{3\hbar^2}{2m}\frac{\partial^2}{\partial r_1^2} + \frac{\partial V}{\partial r_1^2}r_1^2\right)\varepsilon_{AC}^2$$
$$+ \left(-\frac{3\hbar^2}{2m}\frac{\partial^2}{\partial r_2^2} + \frac{\partial V}{\partial r_2^2}r_2^2\right)\varepsilon_{ZZ}^2 + 2\left(\frac{\partial V}{\partial r_1 \partial r_2}r_1 r_2\right)\varepsilon_{AC}\varepsilon_{ZZ} \qquad (7)$$

The retention of second-order terms above enables us to extend the deformation potential theory analysis to larger strain values (i.e., up to 7% in our case), where nonlinearity unavoidably exists. The deformation potential parameters, denoted as $D_{i(j)}$ ($i, j = 1, 2, i \leq j$) below, can thus be determined (see Supporting Information for details)

$$\langle n|H_\varepsilon|n\rangle = D_1\varepsilon_{AC} + D_2\varepsilon_{ZZ} + D_{11}\varepsilon_{AC}^2 + D_{22}\varepsilon_{ZZ}^2 + D_{12}\varepsilon_{AC}\varepsilon_{ZZ} \qquad (8)$$

The strain-induced energy shift at a specific reciprocal point φ can be obtained as

$$\delta E^\varphi = D_1^\varphi\varepsilon_{AC} + D_2^\varphi\varepsilon_{ZZ} + D_{11}^\varphi\varepsilon_{AC}^2 + D_{22}^\varphi\varepsilon_{ZZ}^2 + D_{12}^\varphi\varepsilon_{AC}\varepsilon_{ZZ} \qquad (9)$$

where $D_{i(j)}^\varphi$ ($i, j = 1, 2, i \leq j$) are the deformation potential parameters associated with the point φ. We can then write the strain-induced change in the energy gap between two reciprocal points α and β as

$$\delta E^{\alpha\beta} = D_1^{\alpha\beta}\varepsilon_{AC} + D_2^{\alpha\beta}\varepsilon_{ZZ} + D_{11}^{\alpha\beta}\varepsilon_{AC}^2 + D_{22}^{\alpha\beta}\varepsilon_{ZZ}^2 + D_{12}^{\alpha\beta}\varepsilon_{AC}\varepsilon_{ZZ} \qquad (10)$$

with $D_{i(j)}^{\alpha\beta} = D_{i(j)}^\alpha - D_{i(j)}^\beta$. From eq 10 we see that if the values of $D_{i(j)}^{\alpha\beta}$ are known, then the evolution of the energy gap between α and β under the application of in-plane normal strains can be predicted.

Using those data shown in Figures 4−6, the values of corresponding $D_{i(j)}^{\Gamma'K}$ and $D_{i(j)}^{K'K}$ are determined, listed in Tables S1 and S2 (see Supporting Information for details). Hence, the evolutions of Γ'−K and K′−K gaps of the interface modified 2H-MX$_2$ as functions of ε_{AC} and ε_{ZZ} can be predicted. To verify
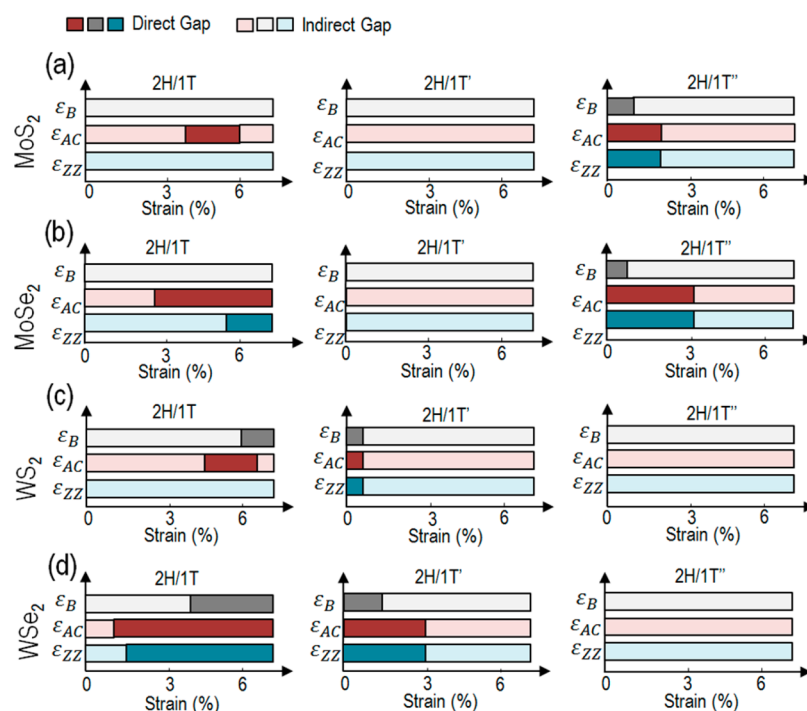
Figure 7. Effects of in-plane strains on bandgap transition for the interface-influenced 2H-MX$_2$ in (a) MoS$_2$, (b) MoSe$_2$, (c) WS$_2$, and (d) WSe$_2$ 2H/1T$^\Psi$ heterostructures. The light gray, red, and blue indicate the ranges of ε_B (biaxial strain), ε_{AC} (uniaxial strain along the armchair direction), and ε_{ZZ} (uniaxial strain along the zigzag direction) corresponding to indirect bandgaps, respectively, while the dark gray, red, and blue indicate the ranges of ε_B, ε_{AC}, and ε_{ZZ} corresponding to direct bandgaps, respectively.

the accuracy of the prediction, two additional sets of DFT calculations were performed: one with $\varepsilon_{ZZ} = 2\varepsilon_{AC}$ and the other with $\varepsilon_{AC} = 2\varepsilon_{ZZ}$. The computed and predicted evolutions of $\Gamma'-K$ and $K'-K$ gaps are compared with each other in Figure 8, showing an excellent agreement. On the basis of our results above, we are able to predict the in-plane normal strain domains in which the interface modified 2H-MX$_2$ exhibits direct and indirect bandgaps, as shown in Figure 9. The boundary between different domains directly corresponds to the threshold strain combination for the bandgap transition. Figure 9 provides a predictive tool to guide the bandgap engineering of a 2H-MX$_2$ monolayer through interface coupling and elastic strain. Furthermore, the above approach can be readily extended to other TMD monolayer systems and their derivatives and is thus of great mechanistic importance to the design of TMD devices.

4. SUMMARY

To conclude, we have systematically studied the electronic properties of four inherent bilayer TMD-MX$_2$ (M = Mo, W, X = S, Se) heterostructures composed of 2H-MX$_2$ and its allotrope 1T$^\Psi$ (1T$^\Psi$ = 1T, 1T', or 1T''). We showed that the 2H-1T$^\Psi$ interface coupling can render the bandgap of 2H-MX$_2$ direct or indirect, along with a modified gap energy. In addition, we found that the bandgap transition of the interface-influenced 2H-MX$_2$ can be modulated by normal in-plane strains. Furthermore, we demonstrated that those inherent heterostructures enrich the means to realize direct bandgap for 2D TMD materials, providing new possibilities beyond the TMD monolayer. Employing the deformation potential theory, the role of strains in band shifting and bending was analyzed and the competition between between K−K and Γ−K energy gaps was clarified. An analytic model was then formulated and
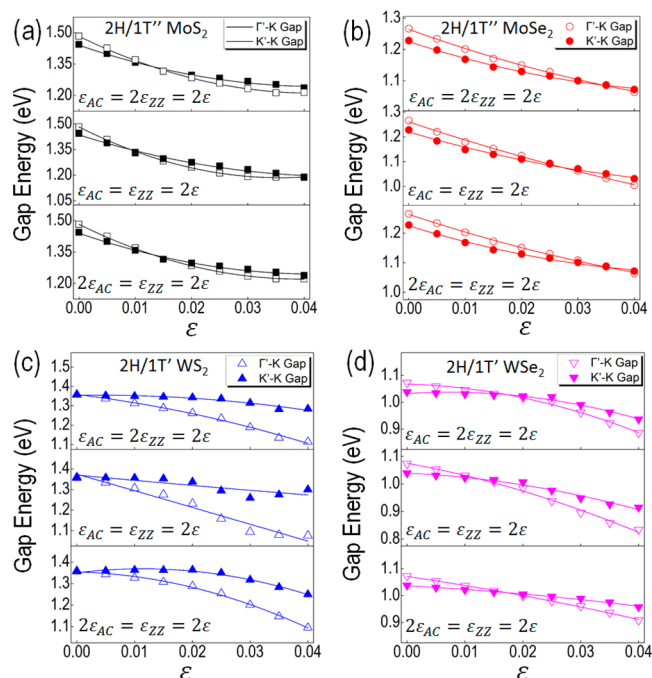

Figure 8. Comparison of the predicted (solid lines) and DFT calculated (symbols) variation of the $\Gamma'-K$ and $K'-K$ gap energies of the interface-influence 2H-MX$_2$ in (a) 2H/1T'' MoS$_2$, (b) 2H/1T'' MoSe$_2$, (c) 2H/1T' WS$_2$, and (d) 2H/1T' WSe$_2$ heterostructures. Three types of strain states, i.e., $\varepsilon_{AC} = 2\varepsilon_{ZZ}$, $\varepsilon_{AC} = \varepsilon_{ZZ}$, and $2\varepsilon_{AC} = \varepsilon_{ZZ}$, are considered for each case.

parametrized, which enables the prediction of bandgap transition for the interface-influenced 2H-MX$_2$ subjected to arbitrary planar normal strains. Our results enrich our
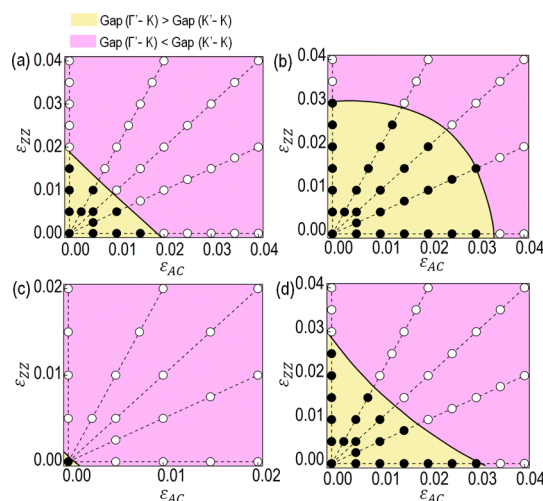
Figure 9. The predicted map of strain domains that correspond to direct (yellow region) and indirect (purple region) bandgaps of the interface-influenced 2H-MX$_2$ in (a) 2H/1T″ MoS$_2$, (b) 2H/1T″ MoSe$_2$, (c) 2H/1T′ WS$_2$, and (d) 2H/1T′ WSe$_2$ heterostructures. The symbols denote the strain states examined via DFT calculations, with black and white ones corresponding to cases where the interface-influenced 2H-MX$_2$ exhibits a larger and smaller Γ′−K gap than the K′−K gap, respectively. The thin dashed lines are drawn for the sole purpose to guide the eyes.

mechanistic knowledge of band structure engineering in TMD materials and suggest a new route to manipulate optical transitions and thus to tune photoluminescence properties of TMD-based devices.

ASSOCIATED CONTENT

ⓢ Supporting Information

The Supporting Information is available free of charge on the ACS Publications website at DOI: 10.1021/acs.jpcc.5b12677.

> Plots of partial charge distributions at CBM and VBM of MoSe$_2$ and WSe$_2$; a table of the ranges of attainable direct bandgap, upon the application of normal in-plane straining, for different 2H-MX$_2$ monolayer and inherent bilayer heterostruccttures; a description of strain-induced band shifting of various bilayer 2H-MX$_2$; and a detailed description of the deformation potential model and fitting of the deformation potential parameters (PDF)

AUTHOR INFORMATION

Corresponding Author

*E-mail: jun.song2@mcgill.ca (J.S.).

Notes

The authors declare no competing financial interest.

ACKNOWLEDGMENTS

REFERENCES

(1) Butun, S.; Tongay, S.; Aydin, K. Enhanced Light Emission from Large-Area Monolayer Mos2 Using Plasmonic Nanodisc Arrays. *Nano Lett.* **2015**, *15*, 2700−2704.

(2) He, Z.; Sheng, Y.; Rong, Y.; Lee, G.-D.; Li, J.; Warner, J. H. Layer-Dependent Modulation of Tungsten Disulfide Photoluminescence by Lateral Electric Fields. *ACS Nano* **2015**, *9*, 2740−2748.

(3) Groenendijk, D. J.; Buscema, M.; Steele, G. A.; Michaelis de Vasconcellos, S.; Bratschitsch, R.; van der Zant, H. S. J.; Castellanos-Gomez, A. Photovoltaic and Photothermoelectric Effect in a Double-Gated Wse2 Device. *Nano Lett.* **2014**, *14*, 5846−5852.

(4) Koppens, F. H. L.; Mueller, T.; Avouris, P.; Ferrari, A. C.; Vitiello, M. S.; Polini, M. Photodetectors Based on Graphene, Other Two-Dimensional Materials and Hybrid Systems. *Nat. Nanotechnol.* **2014**, *9*, 780−793.

(5) Wang, Q.; Xu, K.; Wang, Z.; Wang, F.; Huang, Y.; Safdar, M.; Zhan, X.; Wang, F.; Cheng, Z.; He, J. Van Der Waals Epitaxial Ultrathin Two-Dimensional Nonlayered Semiconductor for Highly Efficient Flexible Optoelectronic Devices. *Nano Lett.* **2015**, *15*, 1183−1189.

(6) Bernardi, M.; Palummo, M.; Grossman, J. C. Extraordinary Sunlight Absorption and One Nanometer Thick Photovoltaics Using Two-Dimensional Monolayer Materials. *Nano Lett.* **2013**, *13*, 3664−3670.

(7) He, K.; Kumar, N.; Zhao, L.; Wang, Z.; Mak, K. F.; Zhao, H.; Shan, J. Tightly Bound Excitons in Monolayer Wse2. *Phys. Rev. Lett.* **2014**, *113*, 026803.

(8) MacNeill, D.; Heikes, C.; Mak, K. F.; Anderson, Z.; Kormányos, A.; Zólyomi, V.; Park, J.; Ralph, D. C. Breaking of Valley Degeneracy by Magnetic Field in Monolayer Mose2. *Phys. Rev. Lett.* **2015**, *114*, 037401.

(9) Mak, K. F.; McGill, K. L.; Park, J.; McEuen, P. L. The Valley Hall Effect in Mos2 Transistors. *Science* **2014**, *344*, 1489−1492.

(10) Radisavljevic, B.; Radenovic, A.; Brivio, J.; Giacometti, V.; Kis, A. Single-Layer Mos2 Transistors. *Nat. Nanotechnol.* **2011**, *6*, 147−150.

(11) Krasnozhon, D.; Lembke, D.; Nyffeler, C.; Leblebici, Y.; Kis, A. Mos2 Transistors Operating at Gigahertz Frequencies. *Nano Lett.* **2014**, *14*, 5905−5911.

(12) Lembke, D.; Bertolazzi, S.; Kis, A. Single-Layer Mos2 Electronics. *Acc. Chem. Res.* **2015**, *48*, 100−110.

(13) Li, X.; Yang, L.; Si, M.; Li, S.; Huang, M.; Ye, P.; Wu, Y. Performance Potential and Limit of Mos2 Transistors. *Adv. Mater.* **2015**, *27*, 1547−1552.

(14) Yang, R.; Wang, Z.; Feng, P. X. L. Electrical Breakdown of Multilayer Mos2 Field-Effect Transistors with Thickness-Dependent Mobility. *Nanoscale* **2014**, *6*, 12383−12390.

(15) Wu, W.; et al. Piezoelectricity of Single-Atomic-Layer Mos2 for Energy Conversion and Piezotronics. *Nature* **2014**, *514*, 470−474.

(16) Reed, E. J. Piezoelectricity: Now in Two Dimensions. *Nat. Nanotechnol.* **2014**, *10*, 106−107.

(17) Zhu, H.; Wang, Y.; Xiao, J.; Liu, M.; Xiong, S.; Wong, Z. J.; Ye, Z.; Ye, Y.; Yin, X.; Zhang, X. Observation of Piezoelectricity in Free-Standing Monolayer Mos2. *Nat. Nanotechnol.* **2014**, *10*, 151−155.

(18) Wu, T.; Zhang, H. Piezoelectricity in Two-Dimensional Materials. *Angew. Chem., Int. Ed.* **2015**, *54*, 4432−4434.

(19) Huang, W.; Luo, X.; Gan, C. K.; Quek, S. Y.; Liang, G. Theoretical Study of Thermoelectric Properties of Few-Layer Mos2 and Wse2. *Phys. Chem. Chem. Phys.* **2014**, *16*, 10866−10874.

(20) Buscema, M.; Barkelid, M.; Zwiller, V.; van der Zant, H. S. J.; Steele, G. A.; Castellanos-Gomez, A. Large and Tunable Photothermoelectric Effect in Single-Layer Mos2. *Nano Lett.* **2013**, *13*, 358−363.

(21) Thakurta, S. R. G.; Dutta, A. K. Electrical Conductivity, Thermoelectric Power and Hall Effect in P-Type Molybdenite (Mos2) Crystal. *J. Phys. Chem. Solids* **1983**, *44*, 407−416.

(22) Tahir, M.; Schwingenschlögl, U. Tunable Thermoelectricity in Monolayers of Mos 2 and Other Group-Vi Dichalcogenides. *New J. Phys.* **2014**, *16*, 115003.

(23) Balandin, A. A. Phonon Engineering in Graphene and Van Der Waals Materials. *MRS Bull.* **2014**, *39*, 817−823.

(24) Mak, K. F.; Lee, C.; Hone, J.; Shan, J.; Heinz, T. F. Atomically Thin Mos2: A New Direct-Gap Semiconductor. *Phys. Rev. Lett.* **2010**, *105*, 136805.

(25) Lu, N.; Guo, H.; Li, L.; Dai, J.; Wang, L.; Mei, W.-N.; Wu, X.; Zeng, X. C. Mos2/Mx2 Heterobilayers: Bandgap Engineering Via Tensile Strain or External Electrical Field. *Nanoscale* **2014**, *6*, 2879−2886.

(26) Gong, Y.; et al. Vertical and in-Plane Heterostructures from Ws2/Mos2Monolayers. *Nat. Mater.* **2014**, *13*, 1135−1142.

(27) Hong, X.; Kim, J.; Shi, S.-F.; Zhang, Y.; Jin, C.; Sun, Y.; Tongay, S.; Wu, J.; Zhang, Y.; Wang, F. Ultrafast Charge Transfer in Atomically Thin Mos2/Ws2 Heterostructures. *Nat. Nanotechnol.* **2014**, *9*, 682−686.

(28) Huang, S.; Ling, X.; Liang, L.; Kong, J.; Terrones, H.; Meunier, V.; Dresselhaus, M. S. Probing the Interlayer Coupling of Twisted Bilayer Mos2 Using Photoluminescence Spectroscopy. *Nano Lett.* **2014**, *14*, 5500−5508.

(29) Duerloo, K.-A. N.; Li, Y.; Reed, E. J. Structural Phase Transitions in Two-Dimensional Mo- and W-Dichalcogenide Monolayers. *Nat. Commun.* **2014**, *5*, 4214.

(30) Sevik, C. Assessment on Lattice Thermal Properties of Two-Dimensional Honeycomb Structures: Graphene, H-Bn, H-Mos2, and H-Mose2. *Phys. Rev. B: Condens. Matter Mater. Phys.* **2014**, *89*, 035422.

(31) Wang, S.; Wang, X.; Warner, J. H. All Chemical Vapor Deposition Growth of Mos2:H-Bn Vertical Van Der Waals Heterostructures. *ACS Nano* **2015**, *9*, 5246−5254.

(32) Lee, G.-H.; et al. Flexible and Transparent Mos2 Field-Effect Transistors on Hexagonal Boron Nitride-Graphene Heterostructures. *ACS Nano* **2013**, *7*, 7931−7936.

(33) Kan, M.; Wang, J. Y.; Li, X. W.; Zhang, S. H.; Li, Y. W.; Kawazoe, Y.; Sun, Q.; Jena, P. Structures and Phase Transition of a Mos2Monolayer. *J. Phys. Chem. C* **2014**, *118*, 1515−1522.

(34) Kappera, R.; Voiry, D.; Yalcin, S. E.; Branch, B.; Gupta, G.; Mohite, A. D.; Chhowalla, M. Phase-Engineered Low-Resistance Contacts for Ultrathin Mos2 Transistors. *Nat. Mater.* **2014**, *13*, 1128−1134.

(35) Voiry, D.; Goswami, A.; Kappera, R.; SilvaCecilia de Carvalho Castro, e.; Kaplan, D.; Fujita, T.; Chen, M.; Asefa, T.; Chhowalla, M. Covalent Functionalization of Monolayered Transition Metal Dichalcogenides by Phase Engineering. *Nat. Chem.* **2014**, *7*, 45−49.

(36) Accounts of Chemical Research; Guo, Y.; Sun, D.; Ouyang, B.; Raja, A.; Song, J.; Heinz, T. F.; Brus, L. E. Probing the Dynamics of the Metallic-to-Semiconducting Structural Phase Transformation in Mos2 Crystals. *Nano Lett.* **2015**, *15*, 5081−5088.

(37) Pandey, M.; Bothra, P.; Pati, S. K. Phase Transition of Mos2 Bilayer Structures. *J. Phys. Chem. C* **2016**, *120*, 3776−3780.

(38) Zhou, Y.; Reed, E. J. Structural Phase Stability Control of Monolayer Mote2 with Adsorbed Atoms and Molecules. *J. Phys. Chem. C* **2015**, *119*, 21674−21680.

(39) Li, Y.; Duerloo, K.-A. N.; Wauson, K.; Reed, E. J. Structural Semiconductor-to-Semimetal Phase Transition in Two-Dimensional Materials Induced by Electrostatic Gating. *Nat. Commun.* **2016**, *7*, 10671.

(40) Ouyang, B.; Lan, G.; Guo, Y.; Mi, Z.; Song, J. Phase Engineering of Monolayer Transition-Metal Dichalcogenide through Coupled Electron Doping and Lattice Deformation. *Appl. Phys. Lett.* **2015**, *107*, 191903.

(41) Enyashin, A. N.; Yadgarov, L.; Houben, L.; Popov, I.; Weidenbach, M.; Tenne, R.; Bar-Sadan, M.; Seifert, G. New Route for Stabilization of 1t-Ws2 and Mos2 Phases. *J. Phys. Chem. C* **2011**, *115*, 24586−24591.

(42) Nayak, A. P.; Bhattacharyya, S.; Zhu, J.; Liu, J.; Wu, X.; Pandey, T.; Jin, C.; Singh, A. K.; Akinwande, D.; Lin, J.-F. Pressure-Induced Semiconducting to Metallic Transition in Multilayered Molybdenum Disulphide. *Nat. Commun.* **2014**, *5*, 3731.

(43) Duerloo, K.-A. N.; Reed, E. J. Structural Phase Transitions by Design in Monolayer Alloys. *ACS Nano* **2016**, *10*, 289−297.

(44) Qian, X.; Liu, J.; Fu, L.; Li, J. Quantum Spin Hall Effect in Two-Dimensional Transition Metal Dichalcogenides. *Science* **2014**, *346*, 1344−1347.

(45) Wu, Z.; Tang, C.; Zhou, P.; Liu, Z.; Xu, Y.; Wang, D.; Fang, B. Enhanced Hydrogen Evolution Catalysis from Osmotically Swollen Ammoniated Mos2. *J. Mater. Chem. A* **2015**, *3*, 13050−13056.

(46) Lukowski, M. A.; Daniel, A. S.; Meng, F.; Forticaux, A.; Li, L.; Jin, S. Enhanced Hydrogen Evolution Catalysis from Chemically Exfoliated Metallic Mos2 Nanosheets. *J. Am. Chem. Soc.* **2013**, *135*, 10274−10277.

(47) Du, H.; Guo, H.-L.; Liu, Y.-N.; Xie, X.; Liang, K.; Zhou, X.; Wang, X.; Xu, A.-W. Metallic 1t-Lixmos2 Cocatalyst Significantly Enhanced the Photocatalytic H2 Evolution over Cd0.5zn0.5s Nanocrystals under Visible Light Irradiation. *ACS Appl. Mater. Interfaces* **2016**, *8*, 4023−4030.

(48) Eda, G.; Fujita, T.; Yamaguchi, H.; Voiry, D.; Chen, M.; Chhowalla, M. Coherent Atomic and Electronic Heterostructures of Single-Layer Mos2. *ACS Nano* **2012**, *6*, 7311−7317.

(49) Cai, L.; et al. Vacancy-Induced Ferromagnetism of Mos2 Nanosheets. *J. Am. Chem. Soc.* **2015**, *137*, 2622−2627.

(50) Lin, Y.-C.; Dumcenco, D. O.; Huang, Y.-S.; Suenaga, K. Atomic Mechanism of the Semiconducting-to-Metallic Phase Transition in Single-Layered Mos2. *Nat. Nanotechnol.* **2014**, *9*, 391−396.

(51) Perdew, J.; Burke, K.; Ernzerhof, M. Generalized Gradient Approximation Made Simple. *Phys. Rev. Lett.* **1996**, *77*, 3865−3868.

(52) Blöchl, P. E. Projector Augmented-Wave Method. *Phys. Rev. B: Condens. Matter Mater. Phys.* **1994**, *50*, 17953−17979.

(53) Benavente, E.; Santa Ana, M. A.; Mendizábal, F.; González, G. Intercalation Chemistry of Molybdenum Disulfide. *Coord. Chem. Rev.* **2002**, *224*, 87−109.

(54) Zhao, W.; Ghorannevis, Z.; Chu, L.; Toh, M.; Kloc, C.; Tan, P.-H.; Eda, G. Evolution of Electronic Structure in Atomically Thin Sheets of WS2 and WSe2. *ACS Nano* **2013**, *7*, 791−797.

(55) Zhao, W.; Ghorannevis, Z.; Amara, K. K.; Pang, J. R.; Toh, M.; Zhang, X.; Kloc, C.; Tan, P. H.; Eda, G. Lattice Dynamics in Mono- and Few-Layer Sheets of Ws2 and Wse2. *Nanoscale* **2013**, *5*, 9677−9683.

(56) Grimme, S.; Ehrlich, S.; Goerigk, L. Effect of the Damping Function in Dispersion Corrected Density Functional Theory. *J. Comput. Chem.* **2011**, *32*, 1456−1465.

(57) Grimme, S. Semiempirical Gga-Type Density Functional Constructed with a Long-Range Dispersion Correction. *J. Comput. Chem.* **2006**, *27*, 1787−1799.

(58) Grimme, S.; Antony, J.; Ehrlich, S.; Krieg, H. A Consistent and Accurate Ab Initio Parametrization of Density Functional Dispersion Correction (Dft-D) for the 94 Elements H-Pu. *J. Chem. Phys.* **2010**, *132*, 154104.

(59) Cheiwchanchamnangij, T.; Lambrecht, W. R. L. Quasiparticle Band Structure Calculation of Monolayer, Bilayer, and Bulk Mos2. *Phys. Rev. B: Condens. Matter Mater. Phys.* **2012**, *85*, 205302.

(60) Mak, K. F.; He, K.; Lee, C.; Lee, G. H.; Hone, J.; Heinz, T. F.; Shan, J. Tightly Bound Trions in Monolayer Mos2. *Nat. Mater.* **2012**, *12*, 207−211.

(61) Cardona, M.; Pollak, F. H. Energy-Band Structure of Germanium and Silicon: The K Mode Centered Method. *Phys. Rev.* **1966**, *142*, 530−543.

(62) Klein, A.; Tiefenbacher, S.; Eyert, V.; Pettenkofer, C.; Jaegermann, W. Electronic Band Structure of Single-Crystal and Single-Layer Ws2: Influence of Interlayer Van Der Waals Interactions. *Phys. Rev. B: Condens. Matter Mater. Phys.* **2001**, *64*, 205416.

(63) Peelaers, H.; Van de Walle, C. Effects of Strain on Band Structure and Effective Masses in Mos2. *Phys. Rev. B: Condens. Matter Mater. Phys.* **2012**, *86*, 241401.

(64) Bardeen, J.; Shockley, W. Deformation Potentials and Mobilities in Non-Polar Crystals. *Phys. Rev.* **1950**, *80*, 72−80.

(65) Dresselhaus, G.; Kip, A. F.; Kittel, C. Cyclotron Resonance of Electrons and Holes in Silicon and Germanium Crystals. *Phys. Rev.* **1955**, *98*, 368−384.

(66) Herring, C.; Vogt, E. Transport and Deformation-Potential Theory for Many-Valley Semiconductors with Anisotropic Scattering. *Phys. Rev.* **1956**, *101*, 944−961.

(67) Kane, E. O. Energy Band Structure in P-Type Germanium and Silicon. *J. Phys. Chem. Solids* **1956**, *1*, 82−99.

(68) Cheiwchanchamnangij, T.; Lambrecht, W. R. L.; Song, Y.; Dery, H. Strain Effects on the Spin-Orbit-Induced Band Structure Splittings in Monolayer Mos2 and Graphene. *Phys. Rev. B: Condens. Matter Mater. Phys.* **2013**, *88*, 155404.